INL EXT-19-56583
Revision 0

Post-irradiation Examinations of Accident Tolerant Fuel Candidates with Iron-alloy Cladding

November 2019

Fabiola Cappia

Changing the World's Energy Future

INL is a U.S. Department of Energy National Laboratory operated by Battelle Energy Alliance, LLC

INL EXT-19-56583
Revision 0

Post-irradiation Examinations of Accident Tolerant Fuel Candidates with Iron-alloy Cladding

Fabiola Cappia

November 2019

Idaho National Laboratory
Characterization and Advanced PIE Division
Idaho Falls, Idaho 83415

http://www.inl.gov

Prepared for the
U.S. Department of Energy
Office of Nuclear Energy
Under DOE Idaho Operations Office
Contract DE-AC07-05ID14517

Page intentionally left blank

SUMMARY

A collaborative effort of the Advanced Fuels Campaign together with industry consortia is focused on the development of enhanced Accident Tolerant Fuels (ATF) for Light Water Reactors (LWRs). The scoping studies, referred to as ATF-1 irradiations, are being performed in the Advanced Test Reactor of Idaho National Laboratory using drop-in style irradiations. The Post-Irradiation Examinations (PIEs) of ATF-1 began in 2017 and continued in 2019. This report describes the results of examinations on ATF-1 irradiations designed to test the performance of iron-based cladding.

Two rodlets with commercial iron-based cladding and UO_2 pellets have been irradiated to low burnup (i.e., < 20 GWd/tHM). The first rodlet had an Alloy33® cladding, while the other had a Kanthal APMT® cladding. The performed PIEs were focused on the determination of fuel microstructure, evaluation of fuel-cladding interaction and irradiation-induced variations of cladding mechanical properties. For both rodlets, no significant changes in the cladding hardness were measured, and the cladding hoop strain remained limited. Gamma tomography revealed no Cs axial migration as expected for LWR fuel, but significant cesium radial migration, which was induced by thermal migration consequent to high irradiation temperatures compared to standard LWR irradiation temperatures. Microstructure analyses revealed formation of secondary phases along the pellet rim of samples from both rodlets. No wastage or extensive chemical interaction between the fuel and the internal wall of the cladding was observed, suggesting that the secondary phases accumulated at the pellet rim might be due to formation of Cs-U-O compounds. However, further advanced PIEs are necessary to confirm this hypothesis.

Page intentionally left blank

CONTENTS

FIGURES

TABLES

ACRONYMS

ATF	Accident Tolerant Fuel
ATR	Advanced Test Reactor
HFEF	Hot Fuel Examination Facility
IMCL	Irradiated Materials Characterization Laboratory
INL	Idaho National Laboratory
LHGR	Linear Heat Generation Rate
MCNP	Monte Carlo N-Particle
NDE	Non-destructive Examination
NRAD	Neutron Radiography (Reactor)
PGS	Precision Gamma Screening
PICT	Peak Inner Cladding Temperature
PIE	Postirradiation Examination

Page intentionally left blank

Post-irradiation Examinations of Accident Tolerant Fuel Candidates with Iron-alloy Cladding

1. INTRODUCTION

In fission nuclear reactors, the fuel cladding is not only a containment providing geometrical stability to the fuel stack, it is also the most important safety barrier as its integrity ensures the retention of fission products and the fuel itself. The selection of fuel cladding material is the result of a balance among several design constraints, e.g. service temperature, stability under irradiation and with coolant chemistry, neutron economy, mechanical strength and toughness just to name a few [1]. Based on these considerations, zirconium-based alloys have been chosen more than forty years ago as the best cladding candidate for water nuclear reactors [2]. Thanks to decades of improvements and optimization, zirconium cladding has reached excellent records of operational reliability [3].

In spite of the successful history of performance, other types of materials are presently being re-considered to replace zirconium alloys [4]. The renewed interest in alternative types of cladding stems from the severe limitations known for Zr-alloy claddings under both design-basis accidents (DBA) and beyond-design-basis accidents (BDBA) [5]. Many of the regulatory requirements and associated operational constraints are driven by failure risks associated with cladding embrittlement due to hydrogen pick-up and oxidation [6]. In addition, hydride re-orientation occurring during drying before final disposal is another area of safety concern, as they increase cladding susceptibility for failure [7]. As hydride concentration generally increases with burnup, this factor poses another constraint on burnup.

The large gain in the safety margin, which can be translated in economic benefit through increased operational flexibility, that is forecasted if these issues can be mitigated is a driving factor in current Research and Development (R&D) efforts aim at developing and qualifying new cladding materials. Among others, e.g., SiC, iron-based alloys have shown promising results in mitigating oxidation kinetics [5]. A variety of steel types have been tested under both accidental and normal operating conditions. Kanthal APMT® variants, commercial steels belonging to the SS-series and Fe-xCr (x = 15%, 20%, 25%) have been tested both in pure steam [8] or hydrogen-steam [9] environment showing improved corrosion resistance compared to Zr-2 and Zr-4. General Electric has selected a few steels for applications in ATF fuels, namely T91, HT9, nano ferritic alloys (NFA), MA956, XM-27, Alloy33® and Kanthal APMT® [10]. All steels overperformed Zr-2 during corrosion tests in prototypical Boiling Water Reactor (BWR) water environment and in steam, particularly above 800°C [8–10].

Experiments reproducing environment that favor “shadow” corrosion, a phenomenon that occurs in BWR reactors, have also been conducted, confirming a general improved corrosion resistance of steel claddings [11]. All of the ferritic alloys evaluated for stress corrosion cracking response had excellent resistance to crack propagation, even under quite aggressive conditions with 2 ppm dissolved O_2 and 30 ppb sulfate or chloride. Alloy33® and APMT® have also been mechanically tested after irradiation with protons up to 5 dpa at 300°C. Hardnening occurred in both materials, more prominently for Alloy33®, providing a first insight on irradiation response of the material [11].

Overall, advanced iron alloys proved to have desirable attributes in terms of improved oxidation resistance, which is a very desirable characteristic to increase coping time in DBA and BDBA that make them promising candidates as accident tolerant cladding. While these tests can give single-effect testing on the material performance, tailored experiments, specifically irradiation experiments, of rodlets comprising both fuel and cladding are necessary to verify compatibility between the two under neutron irradiation. Phase 1 of the Accident Tolerant Fuel Campaign (ATF-1) is the perfect platform to provide first in-reactor testing for down-selecting purposes of this new cladding concepts. The capsule design allows to assess the performance of the complete system cladding-fuel under controlled neutron irradiation. In this framework, General Electric Corporation selected two alloys, Alloy33® and APMT®

for initial testing in the Advanced Test Reactor (ATR) in combination with commercial UO_2 fuel [11]. The low burnup pins have completed irradiation and underwent Postirradiation Examinations (PIEs), which are presented here.

The report is organized as follows. A summary of the ATF-1 irradiation histories and material characterization of the capsules that have completed PIE is outlined in Section 2. The PIE results are presented and discussed in Section 3, whereas Section 4 summarizes the main findings and outlook of this work.

2. SUMMARY OF EXPERIMENT AND IRRADIATION CONDITIONS

2.1 Experiment Test Matrix

The ATF-1 tests are designed to screen ATF concepts prior to full scale test irradiations in a test reactor water loop or in commercial reactors. The ATF-1 capsule tests a fuel compound (e.g., UO_2, U_3Si_2, UN) against a cladding material, and it is useful for investigating both fuel-cladding interaction and general fuel irradiation performance. The AFT-1 drop-in capsule design and specifications have been reported elsewhere [12].

In the case of the present tests, conventional UO_2 fuel was used and the emphasis is on the irradiation performance of new iron-based cladding alloys. The test matrix is generally referred to as ATF-1G tests. The alloys selected for testing were Alloy33® and APMT®, whose nominal compositions are given in Table 1. A total of four rodlets has been fabricated, two for each type of material with two different burnup targets, as reported in Table 2.

Table 1. Nominal composition of the selected cladding alloys.

Alloy	Nominal composition
Alloy33®	33 Cr + 32 Fe + 31 Ni + 1.6 Mo + 0.6Cu + 0.4 N
APMT®	Fe + 22 Cr + 5 Al + 3 Mo

Table 2. Characteristics of the ATF-1 rodlets part of this irradiation campaign.

Rodlet ID	Cladding material	Fuel material	Target burnup (GWd/tHM)
G01	Alloy33®	UO_2	20
G02*	Alloy33®	UO_2	80
G03	Kanthal APMT®	UO_2	20
G04*	Kanthal APMT®	UO_2	80

2.2 Irradiation History

The irradiation history of all ATF-1 capsules including the subjects of this work is recorded in Reference [13]. The as-run neutronic and thermal irradiation histories for each rodlet were calculated by combining the results of neutronic and thermal analysis of each capsule. The heat generation and linear heat generation rate (LHGR) in each capsule is calculated using whole ATR core Monte Carlo n-Particle (MCNP 6.0) simulations coupled with ORIGEN 2.2 for depletion. The recorded ATR power history from each cycle and the initial ATR core loading are used as inputs to these simulations. The heat generation rates are then supplied to a finite element analysis code (Abaqus) to calculate the temperatures in the capsule. The axial variation in power and temperature is only 10-20°C, therefore only maximum temperatures are reported here. For the examined ATF-1G rodlets, the Peak Inner Cladding Temperature (PICT), and fuel centerline temperature histories are recoded in Figure 1 along with the linear heat generation rate (LHGR).

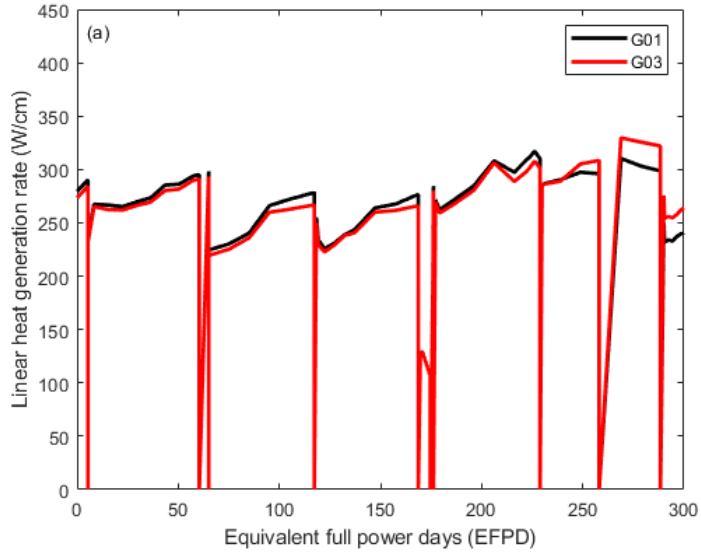
(a)
G01
G03
Linear heat generation rate (W/cm)
Equivalent full power days (EFPD)
0
50
100
150
200
250
300
350
400
450

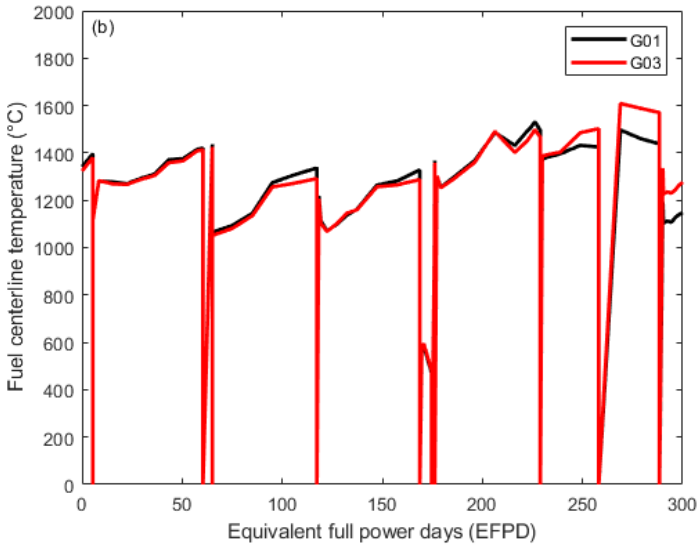
(b)
G01
G03
Fuel centerline temperature (°C)
Equivalent full power days (EFPD)
0
200
400
600
800
1000
1200
1400
1600
1800
2000

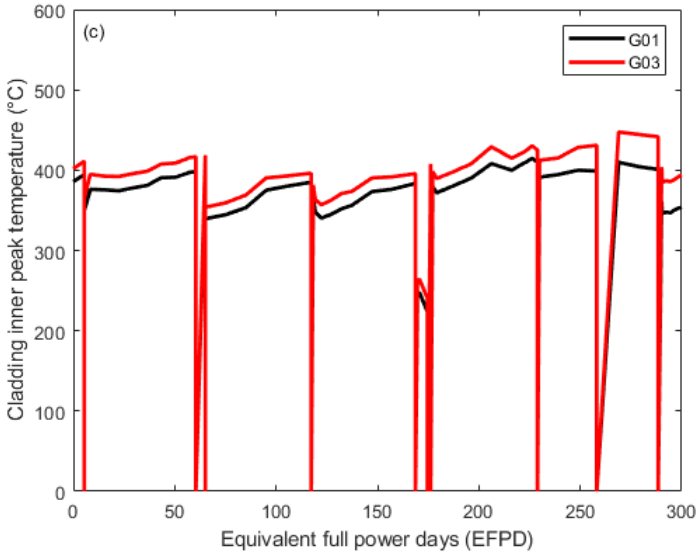

Figure 1. (a) LHGR, (b) fuel centerline and (c) peak cladding inner temperature of ATF-1G G01 and G03.

3. PIE RESULTS

After the rodlets were irradiated at the ATR, PIE was performed at the INL HFEF. Baseline non-destructive PIE performed on the rodlets included visual inspection, neutron radiography, gamma spectrometry and tomography, and dimensional inspection. Details about the techniques can be found in [14]. After capsule examinations, capsule disassembly took place in the containment box in HFEF, and the rodlets underwent NDEs. After NDEs, cross-sections were cut from the mid-axial region of the rodlet to perform optical microscopy and microhardness. Prior to removing the rodlets from the capsules, visual examinations, neutron radiography, and axially resolved gamma spectrometry are performed on the intact capsules. Results from NDEs of the capsules can be found in the previous report [14]. The rodlets were then removed from the capsules, and PIE on the rodlets began.

3.1 Visual Inspection

Visual inspection was performed on the rodlets at different azimuthal angles through the hot cell window. No unusual features were detected on the cladding surface. Representative pictures of the two rodlets are reported in Figure 2.

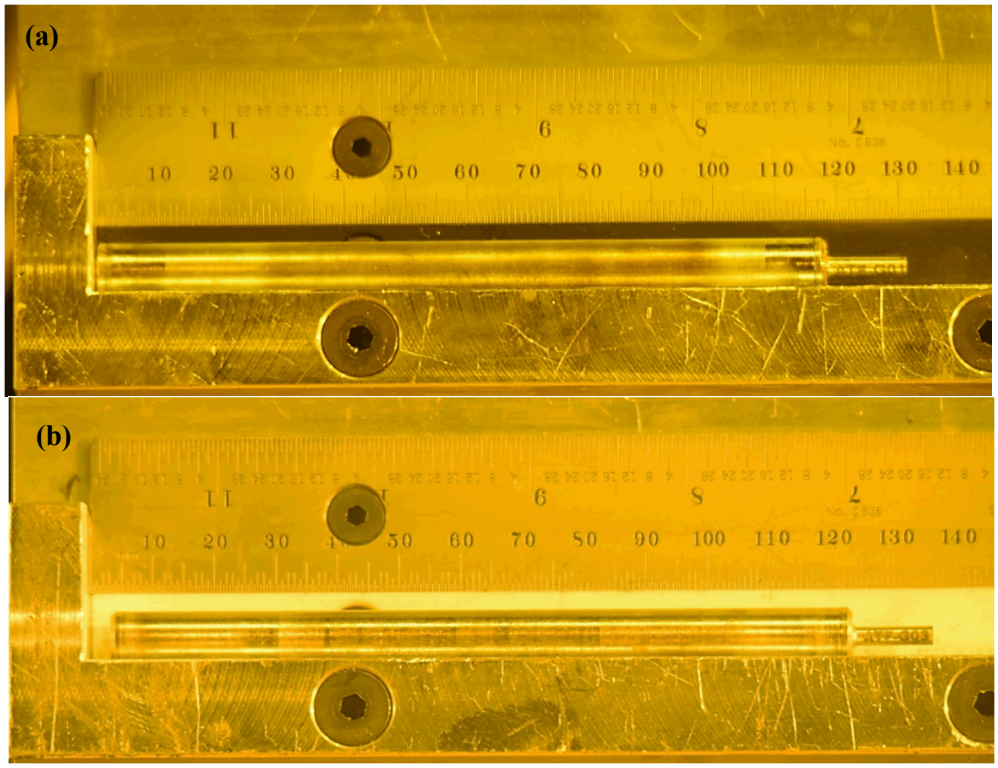

Figure 2. Visual examination of rodlets (a) G01 and (b) G03.

3.2 Neutron Radiography

Neutron radiography of the ATF-1G rodlets was performed using indirect radiography at the NRAD reactor located in HFEF [15]. Radiographs of the rodlets were taken at 6 different angles, each 30 degrees apart. The rodlet radiographs are shown in Figure 3, with the thermal neutron radiograph on the left and the epithermal neutron radiograph on the right. The bottom enriched pellet of the fuel stack in G03 looks severely fractured. The damage occurred during the capsule disassembly, as the neutron radiography of the capsule showed that the pellet was intact [14]. Some cracking of the UO_2 pellet is visible along the full fuel stack, as normally occurs for ceramic fuels. No significant fuel relocation is observed, as expected. No significant axial growth was observed.

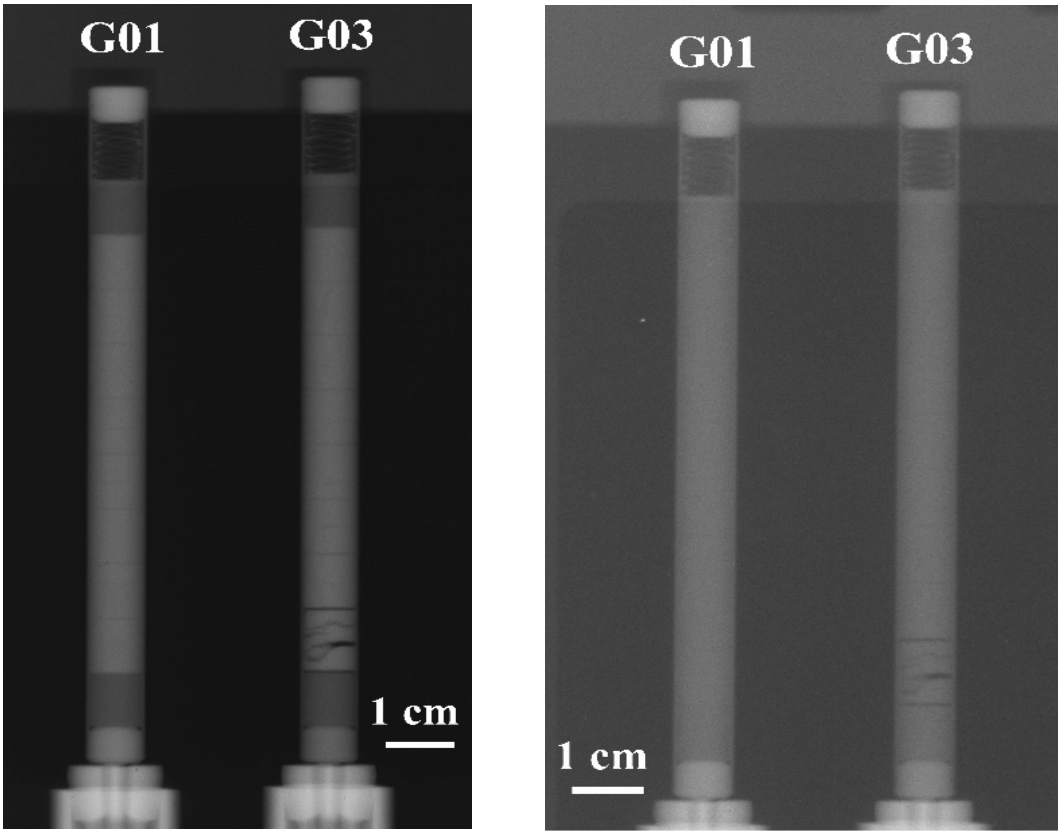

(a) **(b)**

Figure 3. (a) Thermal and (b) epithermal neutron radiographs of ATF-1GE rodlets.

3.3 Dimensional Inspection

Dimensional inspection of the ATF-1G rodlets was performed using a general purpose dimensional inspection device in HFEF. Outside diameter measurements were collected all along the rodlets in 0.5 mm increments axially and at 36 angles every 5 degrees from the initial scan angle to 180 degrees. Diameter measurements are collected with ±5 μm accuracy. The angle-averaged measured diameters for the ATF-1G rodlets is shown in Figure 4 for G01 and Figure 5 for G03. The specified cladding dimension is also shown, including fabrication uncertainty. No significant radial strain of the cladding, resulting in diametral change, was detected in either pins. The diameter value, when including the experimental uncertainty, is within the uncertainty of the as-fabricated values.

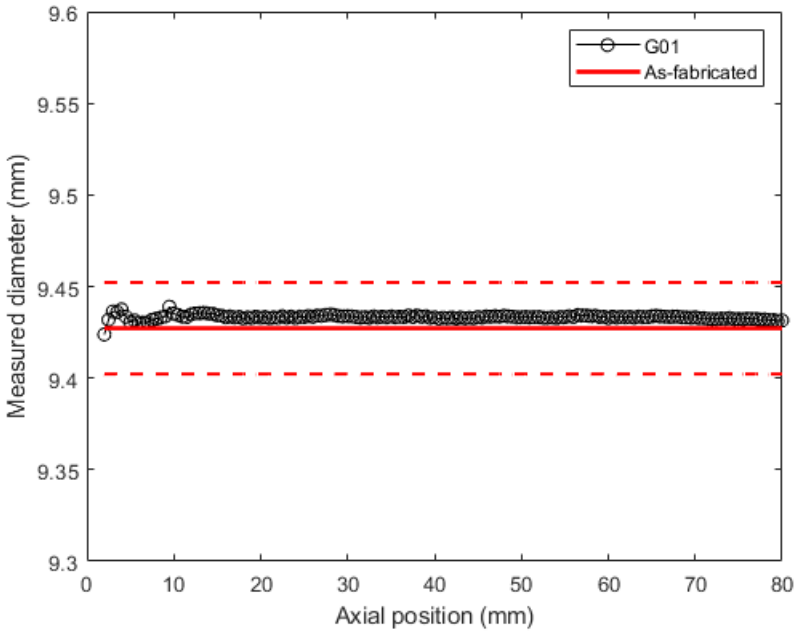

Figure 4. Dimensional measurements of ATF-1G G01. The measured value represents the average of measurements taken every 5°. Red solid lines indicate the nominal values.

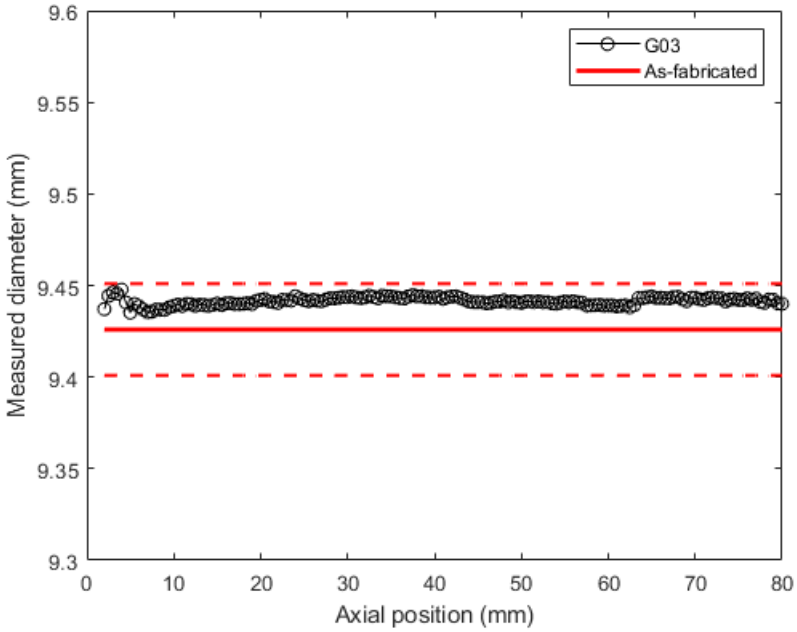

Figure 5. Dimensional measurements of ATF-1G G03. The measured value represents the average of measurements taken every 5°. Red solid lines indicate the nominal values.

3.4 Gamma Spectrometry

Gamma ray spectrometry of the two rodlets was performed using the HFEF Precision Gamma Scanner (PGS). The rodlets were scanned from bottom to top. Axial gamma spectrometry of all the rodlets showed that most detectable fission products did not redistribute axially. Examples of axial distribution of fission products, specifically ^{137}Cs, ^{154}Eu and ^{106}Ru, are reported in Figure 6 and Figure 7 for G01 and G03, respectively. The signal depression at the top and bottom of the fuel stack corresponds to the location of depleted uranium end-pellets. In Figure 8 and Figure 9, some of the activation products, typically created in ferritic steels, are shown. ^{54}Mn is produced from absorption of fast neutrons on ^{54}Fe. As both rodlets experienced similar neutron flux, the higher concentration of ^{54}Mn in rodlets G03 depends mostly on the different initial compositions of the two claddings. ^{60}Co is formed from activation of Ni and Co impurities. The high counts above and below the fuel stack stem from the stainless steel used for welding caps and spring. Increased ^{60}Co activity can be seen in G01, reflecting the Ni content of this alloy.

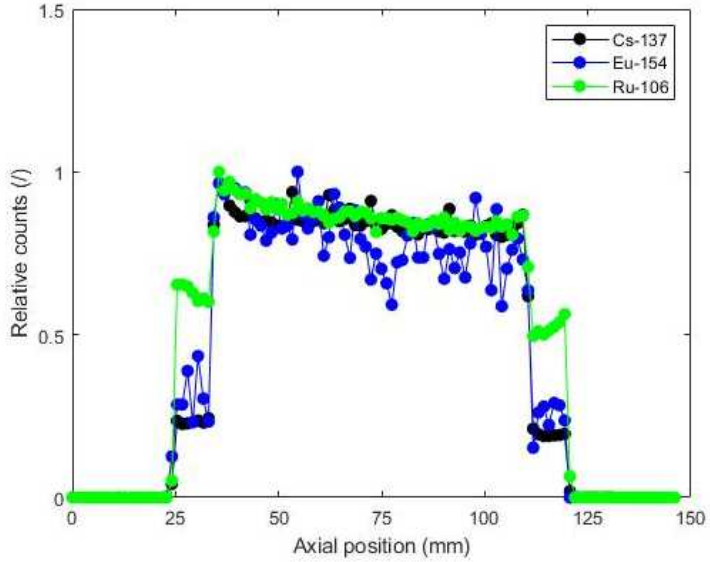

Figure 6. Axial gamma scan of major fission products in rodlet G01.

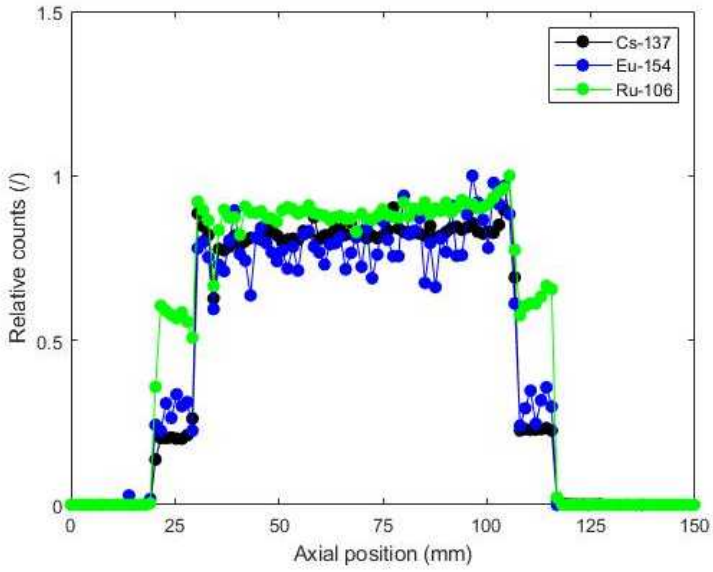

Figure 7. Axial gamma scan of major fission products in rodlet G03.

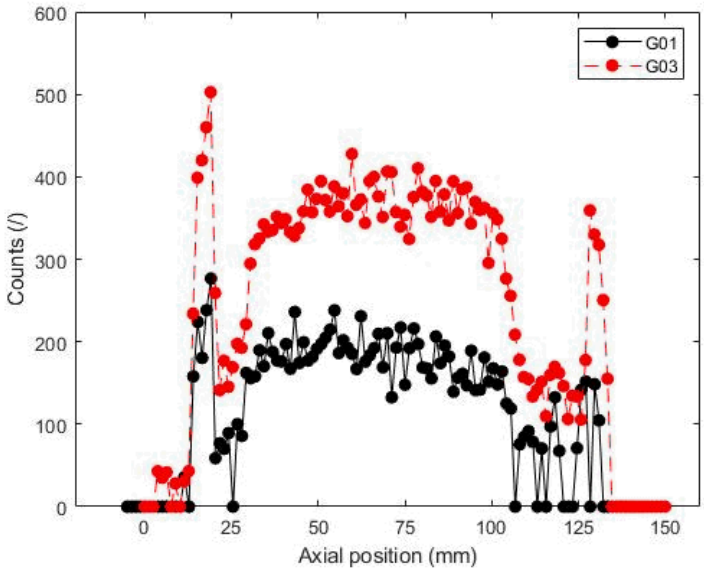

Figure 8. Axial distribution of ^{54}Mn in the two ATF-1G rodlets.

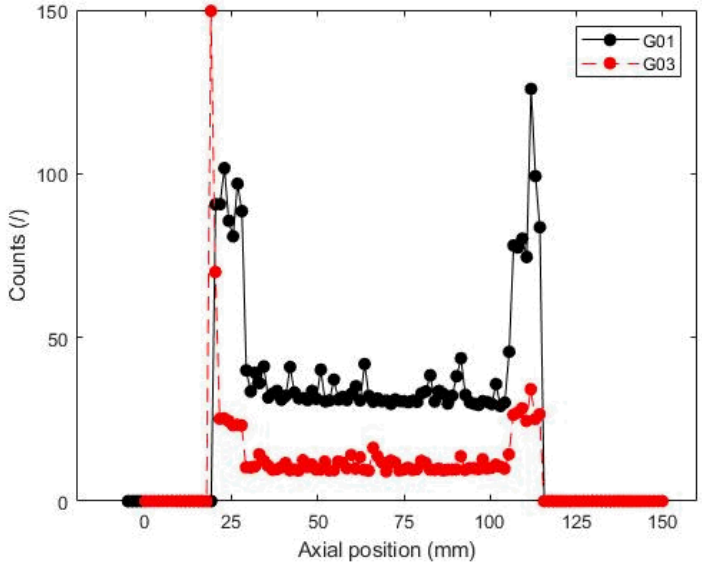

Figure 9. Axial distribution of ^{60}Co in the two ATF-1G rodlets.

In addition to axial gamma spectrometry scans, it is possible to collect two-dimensional distribution of fission products over a specific axial location. This is referred to as Gamma Emission Computed Tomography (GECT), whose details can be found elsewhere [16].

Gamma tomography results of specific fission products are shown in Figure 10. The results are similar for both rodlets. Generally, 16 different angles are collected to obtain the tomography reconstruction, but, for rodlet G03 only 13 angles could be collected due to a system malfunction. This partially impacted the quality of the reconstructed images in Figure 10b, which have increased noise level compared to the results in Figure 10a. Fission products and their daughters that are generally immobile in the fuel matrix, such as ^{144}Ce and ^{95}Nb [17], are homogeneously distributed across the radius. The slight enrichment of the burnup monitors ^{144}Ce and ^{95}Nb is consistent with the increased burnup on the pellet

rim of LWR fuels. The volatile fission product ^{137}Cs shows depletion in the pellet central part for each of the rodlets. Similar results were observed for ^{134}Cs. The behavior is further analyzed in Section 3.4.

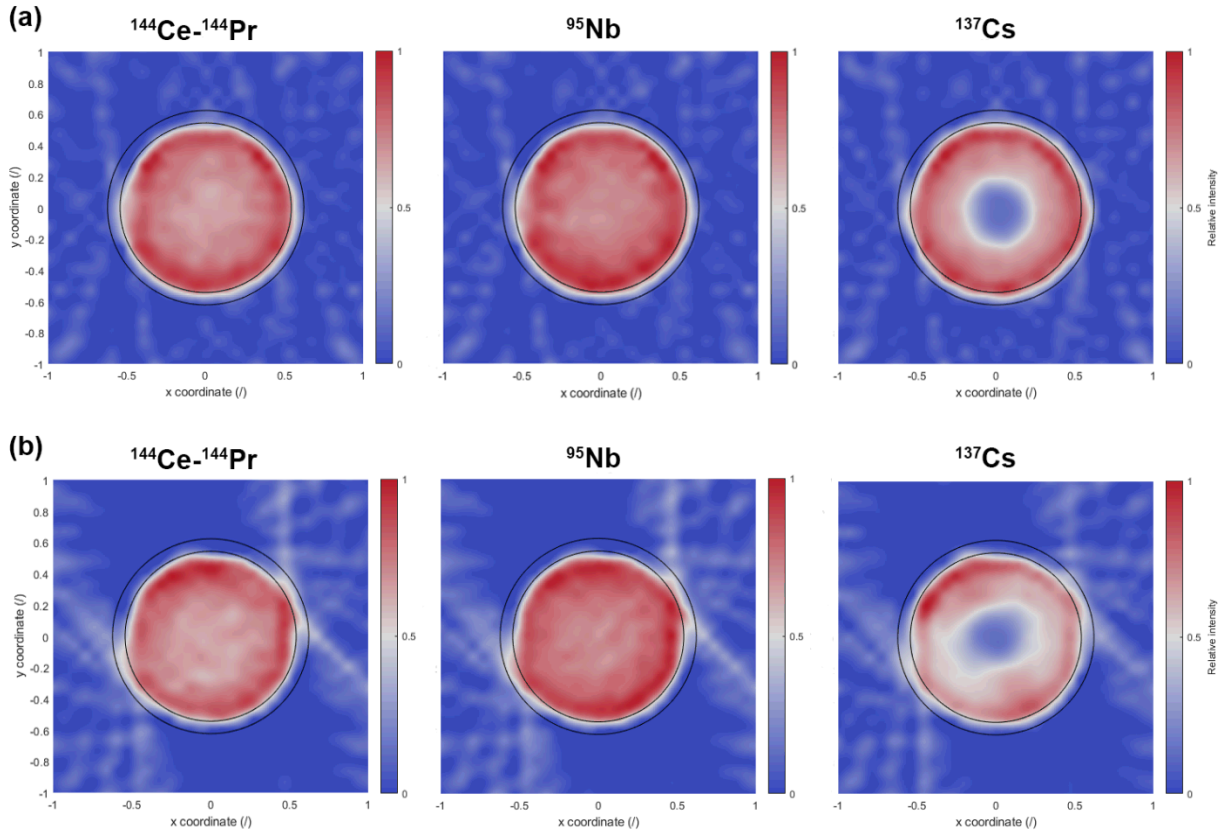

Figure 10. Gamma tomography of selected fission products for (a) G01 and (b) G03.

3.5 Fission Gas Release

Fission gases were collected from the rodlets using the HFEF Gas Assay, Sample, and Recharge (GASR) system. Rodlets were punctured using a 150 W Nd-YAG laser system, and a gas sample was collected in a stainless steel bottle external to the hot cell. Void volume in the rodlet was then determined by a series of backfills into the punctured rodlet and expansions into the GASR system. The rodlet internal gas pressure was derived from the void volume measurement and the initial gas pressure measurement upon puncture. Fission gas compositional analysis was performed by gas mass spectrometry. Results of fission gas analysis provided total elemental composition, krypton isotopic composition, and xenon isotopic composition.

Table 3 summarizes the average calculated fuel centerline irradiation temperature, calculated burnup and fission gas release (FGR) of the two rodlets. Table 4 reports the composition of the detected gas.

Table 3. Fission gas release, calculated average fuel centerline and burnup for ATF-1G.

Rod ID	Fuel Centerline Average Temperature (°C)	Burnup (GWd/tHM)	Fission Gas Release (%)
G01	1253	18.3	7.06 ±0.21
G03	1270	18.3	5.85 ± 0.12

Table 4. Chemical composition of the released gas from ATF-1G rodlets.

Rod ID	Kr (%)	Xe (%)	H2 (%)	He (%)	N (%)	O (%)	Ar (%)	CO2 (%)	Other Gases (%)
G01	8.480	59.800	0.651	28.600	1.380	0.074	0.184	0.785	0.046 ±0.005
	±0.03	±0.4	±0.01	±0.4	±0.06	±0.007	±0.04	±0.05	
G03	7.710	54.300	0.451	36.400	0.140	0.013	0.190	0.710	0.086 ±0.002
	±0.05	±0.4	±0.007	±0.4	±0.01	±0.004	±0.001	±0.003	

3.6 Optical Microscopy

Microscopy samples for investigation of the microstructure were prepared using standard metallographic techniques and examined by a Leica DMi8 microscope installed in the HFEF hot cell. One transverse cross section was prepared from each rodlet, cut from the mid axial position. Mounts overviews from optical microscopy of the pins are shown in Figure 11 and Figure 12. Both pellets are extensively cracked, and the gap appears almost closed. Some areas appear to have high localized porosity (see Figure 13). From the morphology, it is likely that those are a consequence of fabrication inhomogeneities.

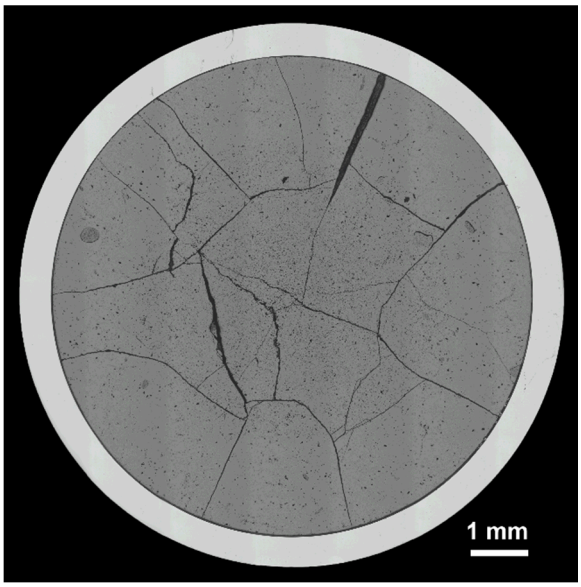

Figure 11. Radial cross section of G01 (50X).

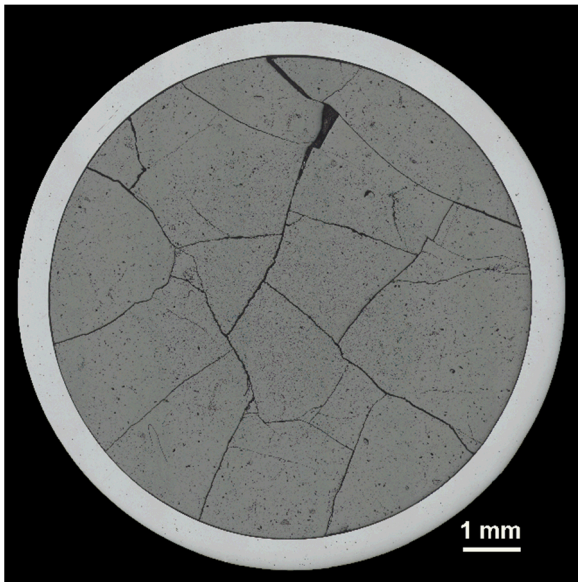

Figure 12. Radial cross section of G03 (50X).

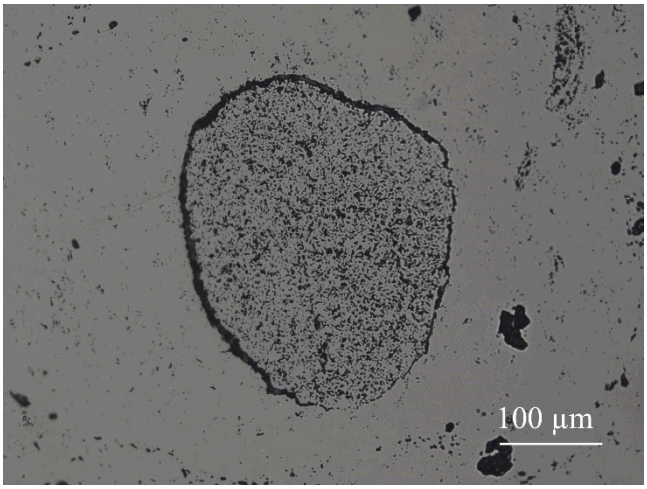

Figure 13. Example of localized porosity observed in the ATF-1G samples.

Secondary phases were observed along the pellet periphery of both rodlets. A representative example is shown in Figure 14a. The thickness of the secondary phase layer increases drastically on the open surface of large cracks, as shown in Figure 14c. No fuel-cladding bonding layer was detected, other than in specific locations in pin G01 as shown in Figure 15. Other than the two specified locations, the cladding inner surface appeared intact and free of wastage, excluding severe corrosion due to the secondary phases or chemical interaction with the fuel.

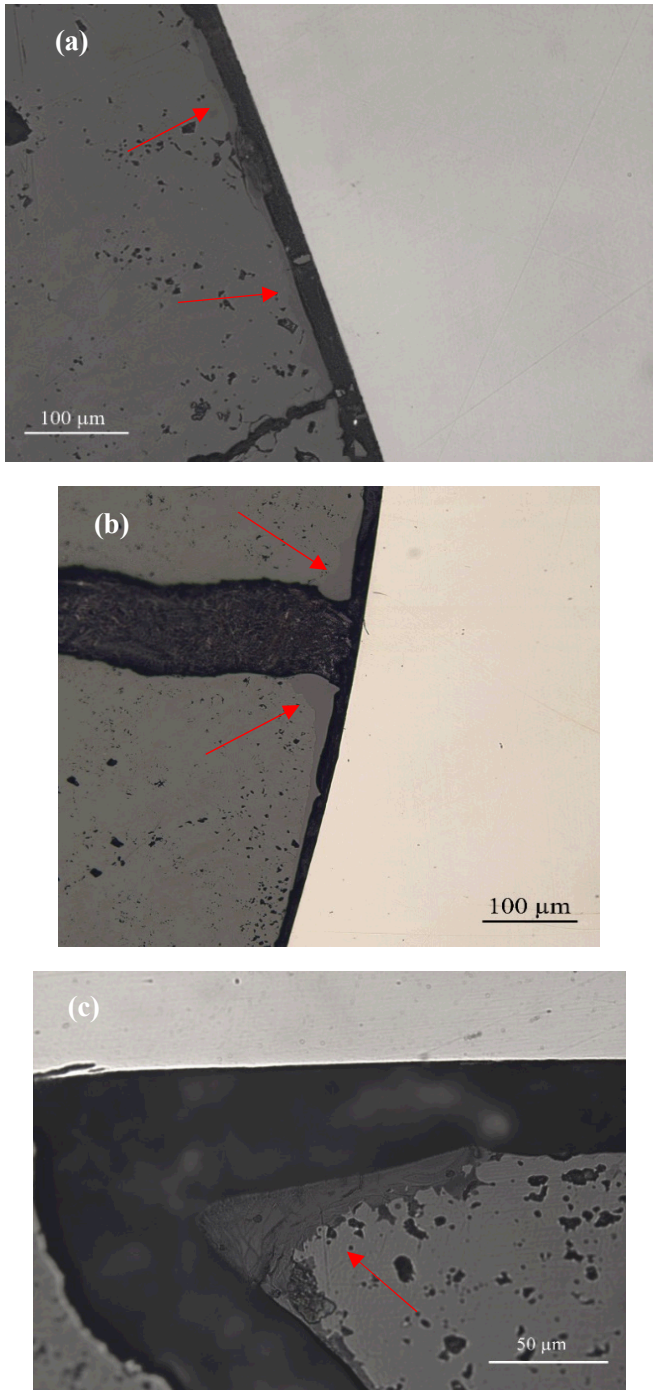

Figure 14. (a) Layer of secondary phases observed on the periphery of the fuel pellets. (b) and (c) highlight the increased thickness of the secondary phase layers close to large cracks open surfaces. (b) was taken from G01, while (c) from G03.

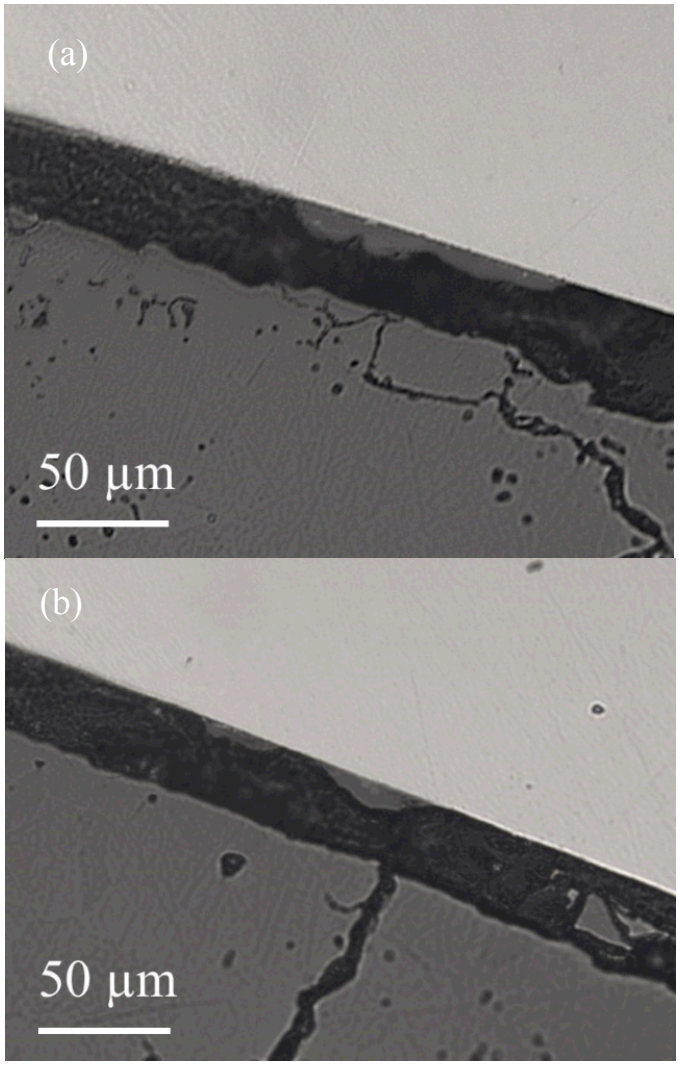

Figure 15. (a)-(b) Localized bonding observed in the sample from rodlet G01.

3.7 Cladding Microhardness

Vickers microhardness measurements were carried out using a LECO AMH55 microscope equipped with a Micro/Macro Vickers Hardness Testing System. The measurements were performed at room temperature under argon protective atmosphere with a load of 50 gf. Dwell time was 13 s. The Vickers hardness number was computed as follows,

$$HV_{0.5} = 0.0018544\frac{P}{d^2} \quad (1)$$

where P (gf) is the applied maximum load and d (µm) is the average length of the two diagonals of the indentation prints. The hardness value was calculated from the average of five indentations at each position along the cladding thickness [18].

Figure 16 and Figure 17 show the profile of the measured Vickers number for Alloy33® (G01) and Kanthal APMT® (G03), respectively. The average Vickers hardness number for the unirradiated alloys is reported along with the uncertainty range [19]. No significant hardening of the alloys was measured. Indentations were made on the zone close to the areas showing significant formation of the secondary phases shown in Figure 14. No local increase in the cladding hardness was measured in the zone.

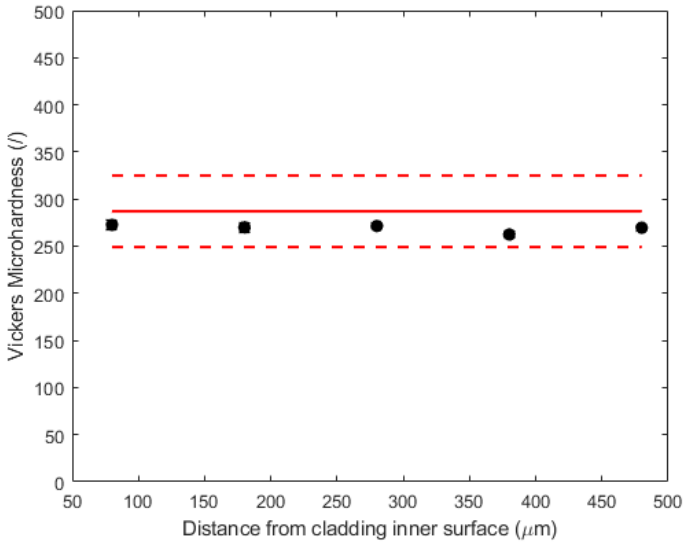

Figure 16. Microhardness profile across the cladding thickness for Alloy33® (G01). The red line represents the measured un-irradiated value and the uncertainty range [19].

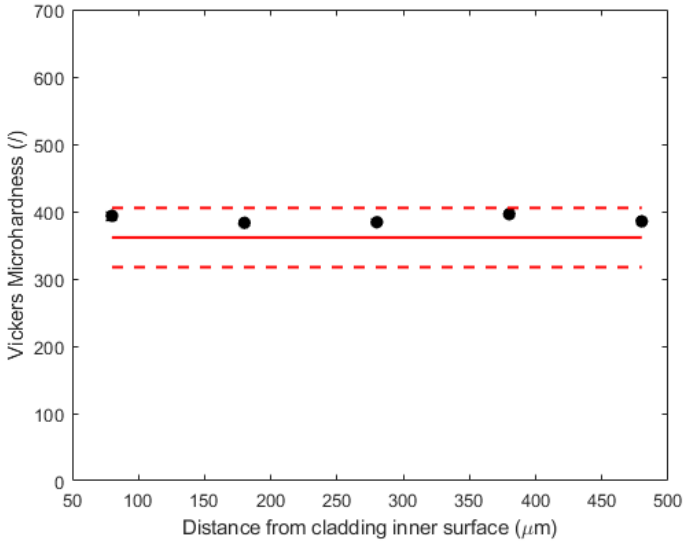

Figure 17. Microhardness profile across the cladding thickness for Kanthal APMT® (G03). The red line represents the measured un-irradiated value and the uncertainty range [19].

4. DISCUSSION

Visual inspection and neutron radiography revealed no anomalies in the ATF-1G rodlets examined to date. Both rodlets experienced very similar irradiation conditions, other than during the last cycle (see Figure 1a). The higher linear power of G03 resulted in a difference of approximately 42°C between the fuel centerline temperatures towards the end of irradiation (Figure 1c). The FGR from G03 was expected to be higher than for G01, as the latter has experienced higher irradiation temperatures. The data in Table 3 show the opposite trend. No obvious differences that could explain the higher FGR (e.g., pronounced cracking) were observed in the microstructure of G01 from optical microscopy. Presently, the observed behavior is not understood, and further analyses are needed.

The higher retained gas in G03, resulting in enhanced swelling compared to G01, could be the reason for the higher hoop strain, which is given by the relative diameter change, observed for the Kanthal cladding (see Figure 8 vs Figure 4). The hoop strain for G03 has an average value of 0.16%, while G01 hoop strain remained below 0.04%. In both cases, the hoop strain is limited.

While axial gamma scanning did not reveal any axial redistribution of fission products (Figure 6 and Figure 7), tomography showed extensive Cs radial migration. The absence of axial redistribution is explained by the lack of large axial thermal gradients occurring in such short pins. Cs release from the central part of the pellet is due to thermally driven diffusion and release. For G01, Cs relative activity is plotted radially against predicted BISON fuel local temperatures [20] in Figure 18. The blue curve represents the fuel temperatures for average LHGR, while the red curve represents the fuel local temperatures for the maximum LHGR. The Cs-depleted region has experienced temperatures exceeding ≈1200°C. Walker et al. [21], performed Electron Probe Micro Analysis (EPMA) on ramp-tested UO_2 fuels and showed that the onset and completion of cesium release corresponded to the 1200°C and 1550°C radial isotherms, respectively [21]. The present results are consistent with what was observed by Walker.

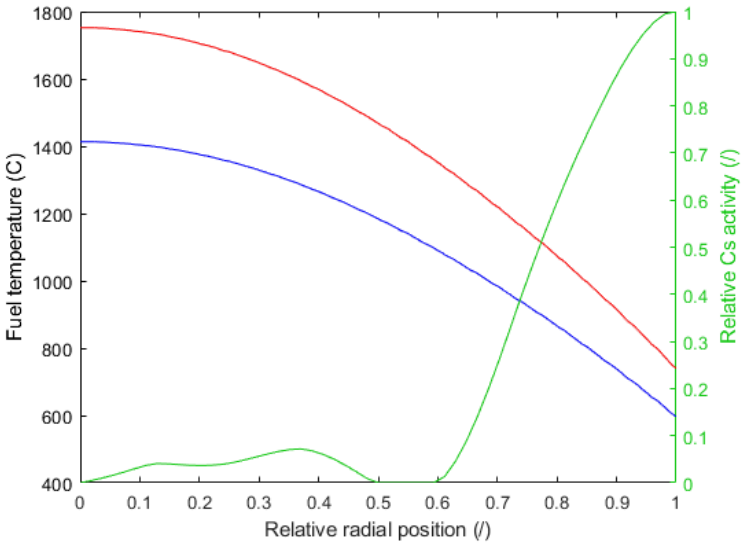

Figure 18. Radial Cs distribution (green line) versus fuel local temperatures for average LHGR (blue line) and maximum LHGR (red line) in G01.

In G01, a layer of secondary phases was observed along the pellet periphery, with increasing thickness corresponding to fuel cracks (Figure 14). The inner surface of the cladding does not show corrosion detectable via optical microscopy, even in the region adjacent to the large deposits. Local

microhardness measurements have been performed in the cladding adjacent to the region shown in Figure 14b, and no localized hardness increase was measured, excluding cladding embrittlement following secondary phases attack. Similarly, a layer of secondary phases was observed along the fuel periphery of G03. It is not known if these phases are a result of cladding components diffusing into the fuel (e.g., Cr or Al) or could be cesium uranate [22] forming after accumulation on the pellet periphery of volatile cesium migrated from the central part of the pellet (Figure 15). Energy Dispersive X-Ray (EDX) analyses are necessary to determine the chemical composition of these phases.

5. CONCLUSIONS

This report summarizes the PIE performed in 2019 on the rodlets that are currently available in HFEF from the General Electric ATF-1 irradiation tests (ATF-1G). Both non-destructive and destructive PIE have been carried out on two rodlets focused on determining the performance of FeCrAl alloys.

The analyses of the ATF-1G irradiations did not show anomalies in the performance of FeCrAl alloys. The claddings showed limited hoop strain; microhardness is consistent with out-of-pile data, and no wastage of the inner cladding surface could be observed. Secondary phases have accumulated on the fuel rim, but it is suspected that those are related to the radial Cs migration, consequent the high irradiation temperatures. Chemical analyses are needed to clarify this hypothesis.

6. REFERENCES

[1] C.R.F. Azevedo, Selection of fuel cladding material for nuclear fission reactors, Eng. Fail. Anal. 18 (2011) 1943–1962. doi:https://doi.org/10.1016/j.engfailanal.2011.06.010.

[2] H.G. Rickover, L.D. Geiger, B. Lustman, History of the development of zirconium alloys for use in nuclear reactors, United States, 1975.

[3] R. YANG, B. CHENG, J. DESHON, K. EDSINGER, O. OZER, Fuel R & D to Improve Fuel Reliability, J. Nucl. Sci. Technol. 43 (2006) 951–959. doi:10.1080/18811248.2006.9711181.

[4] K.A. Terrani, Accident tolerant fuel cladding development: Promise, status, and challenges, J. Nucl. Mater. 501 (2018) 13–30. doi:https://doi.org/10.1016/j.jnucmat.2017.12.043.

[5] K.A. Terrani, S.J. Zinkle, L.L. Snead, Advanced oxidation-resistant iron-based alloys for LWR fuel cladding, J. Nucl. Mater. 448 (2014) 420–435. doi:https://doi.org/10.1016/j.jnucmat.2013.06.041.

[6] Nuclear Energy Agency Organisation for Economic Co-operation and Development, Nuclear Fuel Safety Criteria Technical Review, 2012.

[7] Y.S. Kim, Hydride Reorientation and Delayed Hydride Cracking of Spent Fuel Rods in Dry Storage, Metall. Mater. Trans. A. 40 (2009) 2867–2875. doi:10.1007/s11661-009-0044-6.

[8] T. Cheng, J.R. Keiser, M.P. Brady, K.A. Terrani, B.A. Pint, Oxidation of fuel cladding candidate materials in steam environments at high temperature and pressure, J. Nucl. Mater. 427 (2012) 396–400. doi:https://doi.org/10.1016/j.jnucmat.2012.05.007.

[9] B.A. Pint, K.A. Terrani, M.P. Brady, T. Cheng, J.R. Keiser, High temperature oxidation of fuel cladding candidate materials in steam–hydrogen environments, J. Nucl. Mater. 440 (2013) 420–427. doi:https://doi.org/10.1016/j.jnucmat.2013.05.047.

[10] R.B. Rebak, ADVANCED STEELS FOR ACCIDENT TOLERANT FUEL CLADDING IN COMMERCIAL NUCLEAR REACTORS, in: Adv. Mater. Sci. Environ. Energy Technol. III, 2014.

[11] R.B. Rebak, Ferritic Alloys as Accident Tolerant Fuel Cladding Material for Light W ater Reactors, 2014.

[12] F. Cappia, J.M. Harp, Postirradiation examinations of low burnup U3Si2 fuel for light water reactor applications, J. Nucl. Mater. 518 (2019) 62–79. doi:https://doi.org/10.1016/j.jnucmat.2019.02.047.

[13] C.J. Murdock, B.J. Curnutt, C. Hale, Accident Tolerant Fuels Series 1 (ATF-1) Irradiation Testing FY 2018 Status Report, 2018. NL/EXT-18-51584.

[14] J.M. Harp, F. Cappia, L. Capriotti, Postirradiation Examination of the ATF-1 Experiments - 2018 Status, United States, 2018. doi:10.2172/1484529.

[15] A.E. Craft, D.M. Wachs, M.A. Okuniewski, D.L. Chichester, W.J. Williams, G.C. Papaioannou, A.T. Smolinski, Neutron radiography of irradiated nuclear fuel at Idaho National Laboratory, Phys. Procedia. 69 (2015) 483–490.

[16] J.M. Harp, P.A. Demkowicz, Investigation of the Feasibility of Utilizing Gamma Emission Computed Tomography in Evaluating Fission Product Migration in Irradiated TRISO Fuel Experiments, in: Int. Top. Meet. High Temp. React. Technol. (HTR 2014), WeiHai, China, 2014.

[17] R.S. Forsyth, W.H. Blackadder, N. Ronqvist, Burn-Up Determination by High Resolution Gamma Spectrometry Fission Product Migration Studies, Stockholm, 1967.

[18] Standard method for Vickers indentation hardness of advanced ceramics, (1999).

[19] R.B. Rebak, Ferritic Alloys as Accident Tolerant Fuel Cladding Material for Light Water Reactors, 2014.

[20] P. Medvedev, Private communication, (2019).

[21] C.T. Walker, C. Bagger, M. Mogensen, Observations on the release of cesium from UO2 fuel, J. Nucl. Mater. 240 (1996) 32–42. doi:https://doi.org/10.1016/S0022-3115(96)00477-1.

[22] H. Kleykamp, The chemical state of LWR high-power rods under irradiation, J. Nucl. Mater. 84 (1979) 109–117. doi:https://doi.org/10.1016/0022-3115(79)90154-5.